Electronic properties of hydrogen-doped square-planar nickelates

Xuelei Sui,[1,2] Xiangru Han,[2] Heng Jin,[3,2] Xiaoqiang Wu,[4] Liang Qiao,[5,4,*] Xiaohong Shao,[1] and Bing Huang[2,3,†]

[1]*College of Mathematics and Physics, Beijing University of Chemical Technology, Beijing 100029, China*

[2]*Beijing Computational Science Research Center, Beijing 100193, China*

[3]*Department of Physics, Beijing Normal University, Beijing 100875, China*

[4]*School of Mechanical Engineering, Chengdu University, Chengdu 610106, China*

[5]*School of Physics, University of Electronic Science and Technology of China, Chengdu 611731, China*

(Received 15 September 2023; revised 24 November 2023; accepted 2 April 2024; published 22 April 2024)

The layered square-planar nickelates $R_{n+1}Ni_nO_{2n+2}$ (R: rare-earth element) hold great promise in realizing cupratelike superconductors. While the appearance of zero resistivity is extremely sensitive to the concentration of hydrogen(x) in infinite-layer $Sr_{0.2}Nd_{0.8}NiO_2H_x$, the configurations of many other $Nd_{n+1}Ni_nO_{2n+2}H_x$ and the general roles of H in these systems are still unknown. Using first-principles calculations, we find that H atoms prefer to form staggered one-dimensional chains along the c axis, which are obstructed by the fluorite layer of $Nd_{n+1}Ni_nO_{2n+2}$. Importantly, the charge-transfer energy between O $2p$ and Ni $3d$, one of the key factors determining the superconducting temperature in cuprates, is largely and continuously tunable by n and x in nickelates. Further, from the perspective of orbital hybridization and orbital polarization, the quasi-two-dimensional electronic properties are more pronounced for nickelates with smaller n, potentially facilitating superconductivity. These findings shed light on the general roles of H in controlling electronic properties in nickelates and provide valuable guidance for the experimental preparation of superconducting $R_{n+1}Ni_nO_{2n+2}$ materials.

DOI: 10.1103/PhysRevB.109.155156

I. INTRODUCTION

Square-planar nickelates (SPNs) $R_{n+1}Ni_nO_{2n+2}$ (R: rare-earth element), where n represents the number of NiO_2 planes separated by the fluorite layer (FL) [1–5], are proposed to realize cupratelike superconductors. In 2019, the superconductivity with $T_c \sim 10$ K was realized in Sr-doped $NdNiO_2$ ($n = \infty$), and the hole-doping-dependent superconducting dome is centered near $3d^{8.8}$ orbital filling of Ni [6–10]. Subsequently, due to the natural $3d^{8.8}$ orbital filling of Ni, $Nd_6Ni_5O_{12}$ ($n = 5$) was discovered to be an intrinsic superconductor without Sr doping [11,12]. The more two-dimensional (2D)-like fermiology and the lower density of Nd $5d$ orbitals of $Nd_6Ni_5O_{12}$ compared to (Nd,Sr)NiO_2 indicate a stronger resemblance to cuprates [13–15]. Although controversies still exist regarding the superconducting pairing mechanism in these nickelates [16–24], it is generally believed that the NiO_2 planes, analogous to the CuO_2 planes in cuprates, play decisive roles in the observed superconductivity in nickelates [4,25–36]. Importantly, the discoveries of superconductivity in $n = 5$ and $n = \infty$ indicate that many SPNs can potentially exhibit superconductivity under certain conditions which have not been explored yet.

The superconducting nickelates are prepared by removing the apical oxygen in the parent Ruddlesden-Popper phase $Nd_{n+1}Ni_nO_{3n+1}$ through metal hydride reduction [6–11,37–43], which inevitably introduces a significant amount of H dopants [44–49]. Recently, it has been found that the hidden H atoms play another important role in the emergence of superconductivity in nickelates. The presence of unintentional H dopants in infinite-layer (Nd,Sr)NiO_2 has been predicted theoretically [44–46] and subsequently confirmed experimentally [47]. These H dopants are located at the apical oxygen vacancy sites (AOVs). While it has been found that hydrogen is not an effective donor or acceptor, its presence induces two critical factors. (i) H can effectively modify the orbital hybridization (L) between the anisotropic Ni $3d_{x2-y2}$ orbital and isotropic itinerant interstitial s (IIS) orbital [17,50,51] ($L_{3d-\mathrm{IIS}} \sim t_{3d-\mathrm{IIS}}/\Delta_{3d-\mathrm{IIS}}$ [17,47,52–54], where $t_{3d-\mathrm{IIS}}$ is the hopping strength and $\Delta_{3d-\mathrm{IIS}}$ is the energy difference between Ni $3d_{x2-y2}$ and IIS orbitals). (ii) H can tune the orbital polarization (I_{OP}) between Ni $3d_{x2-y2}$ and $3d_{z2}$. Here, $I_{\mathrm{OP}} = (n_{3dz2}-n_{3dx2-y2})/(n_{3dz2}+n_{3dx2-y2})$, in which n_{3dz2} and $n_{3dx2-y2}$ are the orbital occupation of $3d_{z2}$ and $3d_{x2-y2}$, respectively. (i) and (ii) are observed in the experiments via resonant inelastic x-ray scattering (RIXS) and x-ray absorption spectroscopy (XAS) [47]. These two factors significantly influence the quasi-2D electronic properties of nickelates and may play crucial roles in determining the appearance of superconductivity in a narrow H concentration (x) of (Nd,Sr)NiO_2. Apart from the specific case of $n = \infty$, the potential existence of residual H dopants in other SPNs raises two important questions: What are the doping sites of hydrogen atoms in SPNs as a function of n? What roles do H dopants play in modulating the electronic properties and, subsequently, the superconductivity in SPNs with varying n?

To address these challenging questions, first-principles calculations are conducted on H-intercalated $Nd_{n+1}Ni_nO_{2n+2}$ compounds, covering a range of n values from 3 to 6 and ∞. Our results suggest that regardless of different n, hydrogen

*liang.qiao@uestc.edu.cn

†bing.huang@csrc.ac.cn

atoms consistently occupy the AOV sites. Additionally, in contrast to the continuous one-dimensional (1D) chains in $n = \infty$, hydrogen atoms form obstructed and staggered chains along the out of plane direction for finite n. On the other hand, the charge-transfer energy, an important parameter for evaluating superconducting temperature, gradually decreases with increasing x. Furthermore, the presence of H dopants affects the interaction strength between $3d_{x2-y2}$ and other orbitals (including IIS and $3d_{z2}$), resulting in a decrease in both $L_{3d-\mathrm{IIS}}$ and I_{OP}. Due to the fluorite interface, SPNs with smaller n exhibit more pronounced quasi-2D electronic properties. As a result, systems with smaller n exhibit a broader range of x compared to the experimentally superconducting (Nd,Sr)NiO_2H_x, where $L_{3d-\mathrm{IIS}}$ and I_{OP} meet the critical values for superconductivity. Therefore, the superconductivity of SPNs with smaller n may be less sensitive to H concentration, providing valuable guidelines for the experimental preparation of superconducting $Nd_{n+1}Ni_nO_{2n+2}$ compounds.

II. METHODS

First-principles calculations are performed on square-planar nickelates $Nd_{n+1}Ni_nO_{2n+2}$ using the VASP package [55–57]. The crystal structures are optimized using the Perdew-Burke-Ernzerhof (PBE) [58] exchange-correlation functional. Projector augmented wave (PAW) pseudopotentials [59] are utilized, treating the $4f$ electrons of Nd atoms as core electrons. The in-plane lattice constants for nickelates are determined according to the substrates used in experiments. For $n = 3 - 6$, the lattice constants of the ab plane are fixed to the $NdGaO_3$ substrate ($a = b = 3.86$ Å) [11], while for $n = \infty$, they are fixed to the $SrTiO_3$ substrate ($a = b = 3.91$ Å) [47]. The lattice constant along the c axis and the atomic positions are fully relaxed until the force on each atom is less than 1×10^{-3} eV Å^{-1}. The first Brillouin zone is sampled with a $21 \times 21 \times 23$ ($21 \times 21 \times 4$) Γ-centered special grid for a self-consistent cycle for $n = \infty$ ($n = 3 - 6$), and the kinetic-energy cutoff for the plane-wave basis is set to 620 eV. To clearly illustrate the impact of hydrogen atoms, the band structures of supercells are unfolded to the unit cell [60,61]. Wannier downfolding by the WANNIER90 code [62] is employed to obtain on-site energy differences and hopping parameters, including Nd-5d, Ni-3d, O-2p, and IIS orbitals. The orbital fillings are determined by integrating the density of states (DOS) from negative infinity to the E_{F}. The van der Waals correction is adopted [63], and on-site Hubbard U (U= 4 eV) [64] (introduced by Dudarev *et al.* [65]) is applied on the 3d orbitals of Ni atoms. We note that all results are obtained without considering magnetism [66,67]. Phonon calculations are done with the frozen phonon method using the PHONOPY code [68].

III. RESULTS AND DISCUSSION

As a typical example of $Nd_{n+1}Ni_nO_{2n+2}$, Fig. 1(a) shows the crystal structure of $Nd_6Ni_5O_{12}$, which consists of five Ni-O planes within one block. The Ni atoms with one (two) neighboring NiO_2 planes are labeled as Ni_{out} (Ni_{in}). The residual electrons around the AOV site form IIS orbitals [17,47] (Fig. 5 in the Appendix). Without loss of generality, the electronic properties of $Nd_{n+1}Ni_nO_{2n+2}$ are calculated for

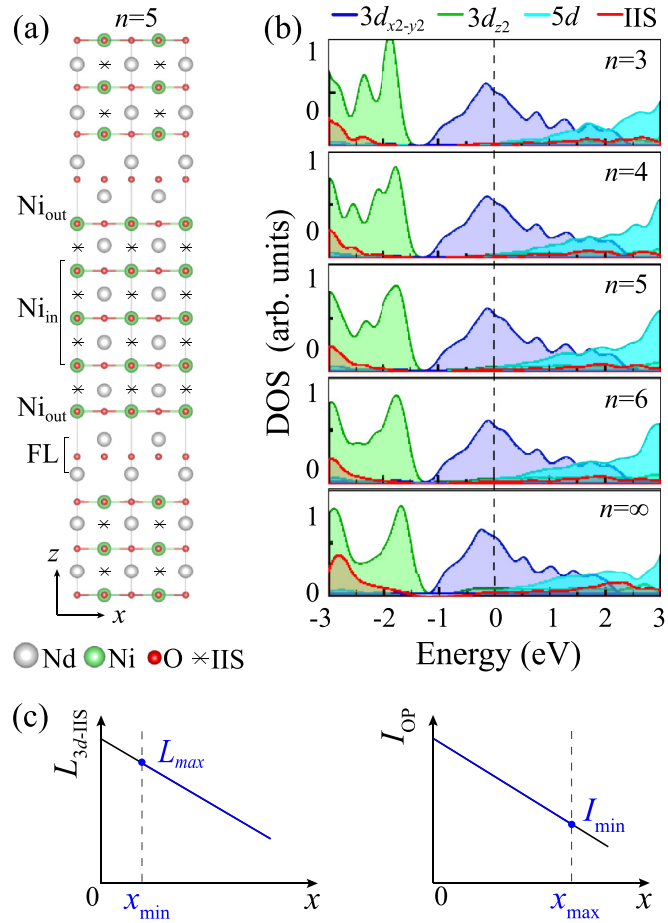

FIG. 1. (a) Crystal structure of $Nd_6Ni_5O_{12}$. The Ni atoms neighboring FL are labeled as Ni_{out}, and others are labeled as Ni_{in}. (b) PDOS for $Nd_{n+1}Ni_nO_{2n+2}$ ($n = 3 - 6$ and ∞). The Fermi level is set to the optimal $3d^{8.8}$ filling of Ni. PDOS for the IIS state is amplified by 2. (c) Schematic illustration of orbital hybridization $L_{3d-\mathrm{IIS}}$ and orbital polarization I_{OP} as functions of H concentration x based on experimental measurements for the $n = \infty$ case [47]. The maximum $L_{3d-\mathrm{IIS}}$ (L_{max}) and minimum I_{OP} (I_{min}) are determined by the experimental superconducting critical x, namely, x_{min} (minimum x) and x_{max} (maximum x), respectively.

$n = 3 - 6$, and ∞. The projected densities of states (PDOS) for the major orbitals, including Ni $3d_{x2-y2}/3d_{z2}$, IIS, and Nd 5d orbitals, are given in Fig. 1(b). On one hand, these compounds share remarkable similarities in the PDOS [2,13–15,69]. In all systems, the $3d_{x2-y2}$ orbital plays a leading role around the Fermi energy. The Ni $3d_{z2}$ (Nd 5d) orbital is almost filled (empty), forming peaks below (above) the Fermi level, and the proportion of IIS orbitals is relatively small. One the other hand, as n increases, the in-plane $3d_{x2-y2}$ orbital remains largely unchanged, while the energy of the out of plane $3d_{z2}$ orbital experiences a slight upward shift, forming a noticeable variation around −2.5 eV. This behavior is partially attributed to the quantum confinement effect induced by the presence of FL [Fig. 1(a)], which splits the $3d_{z2}$ orbitals. The smaller the n, the stronger the confinement effect. Therefore, as n increases, the upward shift of the $3d_{z2}$ orbital leads to a decrease in I_{OP}.

While no consensus has been reached on the superconducting mechanism of nickelates, the resemblance of the crucial

in-plane $3d_{x2-y2}$ orbital between nickelates and cuprates implies similarities between them. In cuprates, the presence of the Cu $3d_{x2-y2}$ orbital near E_F is believed to benefit its superconductivity, while the contributions of other orbitals such as the $3d_{z2}$ and $4s$ orbitals are considered detrimental to d-wave superconductivity [53,70]. In other words, the 2D character of $3d_{x2-y2}$ facilitates the superconductivity. In nickelates, the 2D character of $3d_{x2-y2}$ is largely destroyed. Apart from the occupation of the Ni $3d_{z2}$ orbital, there is also a certain proportion of IIS orbitals present around E_F. The IIS orbitals hybridize with Ni $3d_{x2-y2}$, which not only screens the local moment of Ni atoms [17] but also plays a role in the transition of pairing symmetry [71,72]. In addition, the experimental observations reveal the distinct excitation of the $3d$-IIS hybridized state exclusively in the optimally H-doped nickelates, suggesting a potential connection between IIS orbitals and superconductivity [47]. As the intercalated hydrogen atoms lead to the annihilation of IIS orbitals, the hybridization strength between Ni $3d_{x2-y2}$ and IIS depends largely on x [44–47].

As depicted in Fig. 1(c), as x increases, there is an effective inhibition of local interlayer hopping between IIS and Ni $3d$ orbitals, leading to a decrease in the $L_{3d-\mathrm{IIS}}$. Consequently, it gives rise to a more 2D-like electronic structure mimicking the situation in cuprates. Meanwhile, as x increases, the decreasing occupation of the $3d_{z2}$ orbital reduces the I_{OP}, transforming the electronic structure back to be more 3D-like. Combining the experimental observations [47], a picture can be established in (Nd,Sr)NiO_2H_x: the decrease of $L_{3d-\mathrm{IIS}}$ competes with the decrease of I_{OP}, affecting the 2D character of the $3d_{x2-y2}$ orbital. In the optimal doping region, a quasi-2D electronic structure is formed, which may facilitate superconductivity. As indicated by the dashed lines in Fig. 1(c), the critical maximum $L_{3d-\mathrm{IIS}}$ (L_{max}) is determined by the minimal value of x (x_{min}), while the critical minimum I_{OP} (I_{min}) is determined by the maximal value of x (x_{max}). Considering the similar electronic structures illustrated in Fig. 1(b), it is reasonable to infer that the investigations on the properties of $L_{3d-\mathrm{IIS}}$ and I_{OP} in finite nickelates are crucial, which may provide valuable insights into the determination of superconducting regions of x_{min}–x_{max} experimentally in $Nd_{n+1}Ni_nO_{2n+2}H_x$.

Structure. Test H atoms are located either at high-symmetry positions or random low-symmetry positions. Results show that the intercalated hydrogen atoms occupying AOV sites have the lowest energy (Fig. 6 in the Appendix). The binding energy of the H atoms in $Nd_{n+1}Ni_nO_{2n+2}$ is always negative, regardless of the chemical potential of H (Table I in the Appendix). Therefore, the maximum number of H atoms residing in $Nd_{n+1}Ni_nO_{2n+2}$ is $n-1$ when all AOV sites are occupied. Second, taking $Nd_6Ni_5O_{12}H_{4x}$ with a $2\times2\times1$ supercell as an example, both the in-plane and out of plane arrangement of H are investigated. The lowest-energy configurations are shown in Fig. 2. In each quintuple NiO_2 block, H atoms prefer to form 1D chains along the c axis to maximally recover the local octahedral structure. However, the H chains are obstructed by the presence of FL, and the two H chains in the neighboring blocks are staggered by (0.5, 0.5, 0.5). Meanwhile, the H chains separate Ni atoms in two different local environments, namely, $Ni_{out}O_4H$ and $Ni_{in}O_4H_2$ (Fig. 7 in the Appendix). In the xy plane, H atoms tend to distribute

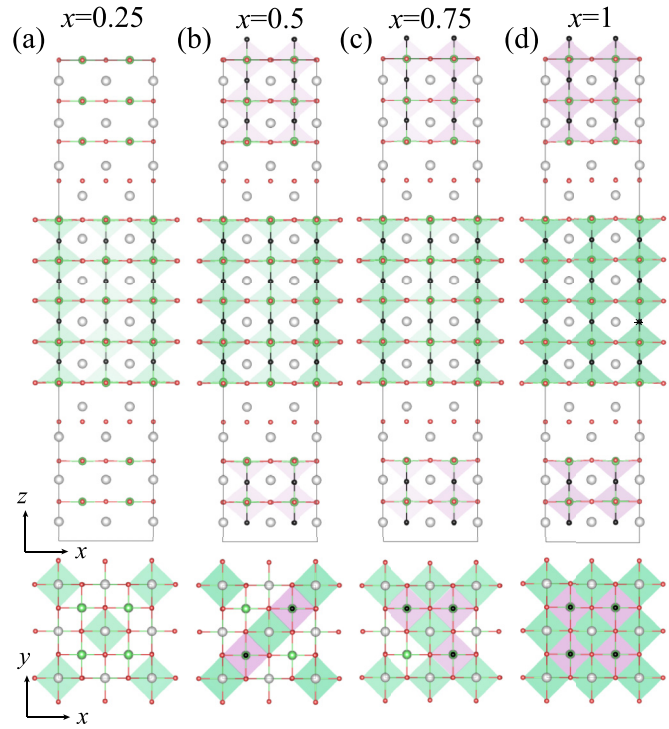

FIG. 2. Side views (upper panels) and top views (lower panels) of the lowest-energy configurations for (a) $Nd_6Ni_5O_{12}H_1$, (b) $Nd_6Ni_5O_{12}H_2$, (c) $Nd_6Ni_5O_{12}H_3$, and (d) $Nd_6Ni_5O_{12}H_4$. Polyhedra highlight the local $Ni_{out}O_4H$ or $Ni_{in}O_4H_2$ environment. Green and pink colors distinguish the existence of H atoms in different blocks.

along the (1 1 0) direction and bond with Nd $5d_{xy}$ orbitals. For example, for $x=0.25$ [Fig. 2(a)], the configuration with two H chains distributing along the (1 1 0) direction in one quintuple NiO_2 layer has the lowest energy, which is 0.15 eV lower than the configuration with one chain in each quintuple layer. For $x=0.5$ [Fig. 2(b)], two H chains distributing along the (1 1 0) direction in both quintuple layers is the ground-state configuration. The dynamic stability is confirmed by the positive phonon frequencies for different x configuration, as shown in Fig. 8. The high-frequency vibration modes ranging from $\sim$ 26 to 49 THz are mainly contributed by hydrogen with light mass. These modes can be experimentally detected through phonon measurements, providing a means to confirm the existence of hydrogen [73].

Electronic structure. First, it is necessary to compare the band structures of $Nd_{n+1}Ni_nO_{2n+2}$ without hydrogen insertion. For instance, when comparing the cases of $n=3$ [Fig. 3(a)] and $n=5$ [Fig. 3(b)], four remarkable features can be identified. (1) The primary characteristics of the band structures are similar, as also noted in Fig. 1(b). (2) The electron pockets of Nd $5d$ orbitals at the Γ point and IIS at the M point are remarkably enhanced in the case of $n=5$, suggesting the increased importance of Nd $5d$ orbitals and IIS in systems with larger n. (3) The electronic structures become more 2D-like with decreasing n due to the decoupling between neighboring NiO_2 blocks along the c axis with the existence of FL. This can be reflected from the similar band dispersion along the $k_z=0$ and $k_z=\pi$ planes, and from the flatter band dispersion of $3d_{z2}$ orbital along the Γ-Z line for

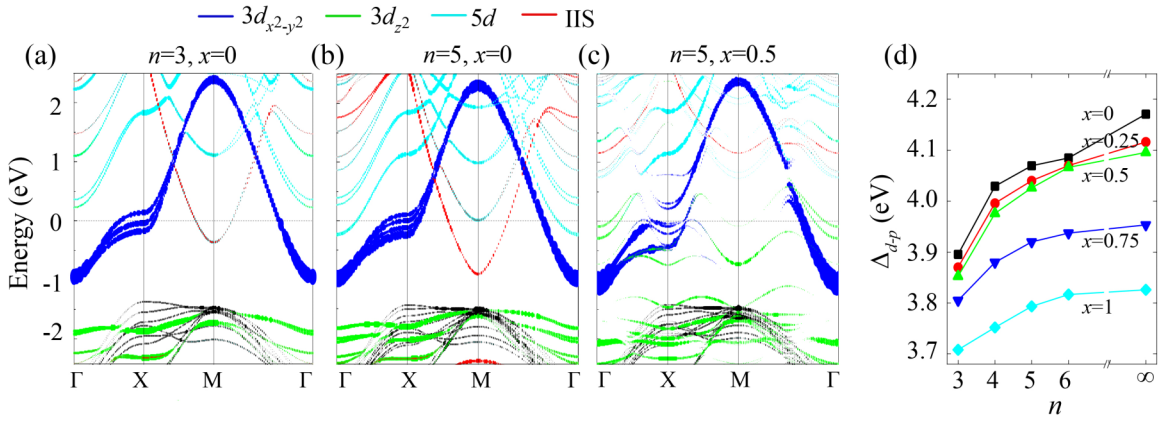

FIG. 3. Projected band structures for (a) $Nd_4Ni_3O_8$, (b) $Nd_6Ni_5O_{12}$, and (c) $Nd_6Ni_5O_{12}H_2$ in the $k_z = 0$ plane. IIS state is amplified by a factor of 2. The Fermi level is set to zero. (d) Charge-transfer energy Δ_{d-p} versus n and x.

smaller n (Fig. 9 in the Appendix) [74,75]. (4) Moreover, despite the different number of neighboring NiO_2 planes of Ni_{in} and Ni_{out}, the $3d_{x2-y2}$ orbitals of both Ni_{in} and Ni_{out} are primarily coupled with the in-plane O $p\sigma$ orbitals (see Fig. 10 in the Appendix).

With the H intercalation, three noticeable variations can be observed from the comparison between Figs. 3(b) and 3(c). (1) The intensity of IIS decreases remarkably. (2) The energy position of Ni $3d_{z2}$ orbital shifts significantly toward the E_F as a result of strong hybridization with the H $1s$ orbital. This strong hybridization leads to a considerable decrease of the I_{OP}, which will be discussed later [47,48]. (3) The energy splitting between the five $3d_{x2-y2}$ orbitals increases, particularly at the X point around E_F. The higher (lower) energy bands are mainly contributed by the Ni_{out} (Ni_{in}) atoms. This is attributed to the different local environments of Ni_{out} ($Ni_{out}O_4H$) and Ni_{in} ($Ni_{in}O_4H_2$). The smaller bonding strength between Ni $3d_{z2}$ and the H $1s$ orbital in the local $Ni_{out}O_4H$ environment results in a smaller downshift of the Ni_{out} $3d_{x2-y2}$ orbital than those of Ni_{in} (for more details, see Fig. 11 in the Appendix). These changes in band structures upon H intercalation give rise to substantial changes in the Fermi surface, as illustrated in Fig. 12.

In cuprates, the hybridization strength L_{p-d} between the O $2p\sigma$ and Cu $3d_{x2-y2}$ orbitals is an important parameter to evaluate the superconductive T_c [53,76]. The charge-transfer energy Δ_{d-p} (on-site energy difference between the Ni $3d_{x2-y2}$ orbital and the O $p\sigma$ orbital), which is inversely proportional to the $p-d$ hybridization strength L_{p-d}, is given in Fig. 3(d). Varying with different n and x, two general trends are observed. (1) For a given x, the Δ_{d-p} increases as n increases, suggesting the decrease of L_{p-d}. Specifically, the calculated Δ_{d-p}'s for $x = 0.25$ are 3.87, 4.04, and 4.12 eV for $n = 3$, 5, and ∞, respectively. These values are in line with previous works [13,27,77]. When $n > 6$, the value of Δ_{d-p} is close to approaching saturation. Interestingly, the similar values of U (~ 4 eV for nickelates [78]) and Δ_{d-p} ($\sim 3-5$ eV) put the $Nd_{n+1}Ni_nO_{2n+2}$ between the charge-transfer and Mott-Hubbard regimes, different from the charge-transfer regime in cuprates ($U \gg \Delta_{d-p}$) [79,80]. Here we note that the Δ_{d-p} is obtained using the DFT+U method, and its value changes slightly when using the DFT method (Fig. 13 in the Appendix). (2) For a given n, the Δ_{d-p} decreases significantly as x increases. For instance, considering $n = 5$, the calculated Δ_{d-p}'s are 4.04, 4.03, 3.92, and 3.79 eV under $x = 0.25$, 0.5, 0.75, and 1, respectively. This variation is primarily attributed to the decreased energy of the $3d_{x2-y2}$ orbital and the increased energy of the $p\sigma$ orbital caused by the H intercalation. Since Δ_{d-p} is a key parameter associated with the value of T_c, where a smaller Δ_{d-p} typically corresponds to a larger T_c, it is expected that the T_c of SPNs could be tuned by n and x. Indeed, this is the case observed in existing experiments. For example, it has been observed that the T_c is slightly smaller in the $n = \infty$ case ($\sim$ 10 K) [6,7,47] compared to the $n = 5$ case ($\sim$ 15 K) [11], attributing to the larger Δ_{d-p} value in the $n = \infty$ case.

H-tuning 2D character of SPNs. It is intriguing to further investigate the effect of interplay between x and n on the 2D character of the electronic structures, specifically the L_{3d-IIS}

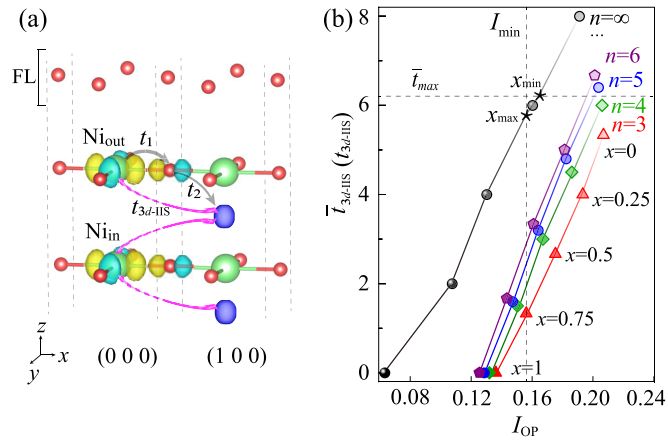

FIG. 4. (a) Schematic intercell hopping between Ni $3d_{x2-y2}$ orbital and IIS orbital (t_{3d-IIS}) via O $p\sigma$ orbital for Ni_{out} and Ni_{in} atoms. Only intercell hopping along the (1 0 0) direction is plotted as an example. Nd atoms are not displayed. (b) Averaged hopping strength $\bar{t}_{3d-IIS}$ and I_{OP} changing as n and x. For a given n, five x ($x = 0$, 0.25, 0.5, 0.75, 1) are given and the symbols become darker for larger x. The experimentally determined x_{min} ($\sim$ 0.22) and x_{max} ($\sim$ 0.28) for the superconducting dome in (Nd,Sr)NiO_2 are labeled, along with the corresponding maximum $\bar{t}_{3d-IIS}$ ($\bar{t}_{max}$) and I_{min}.

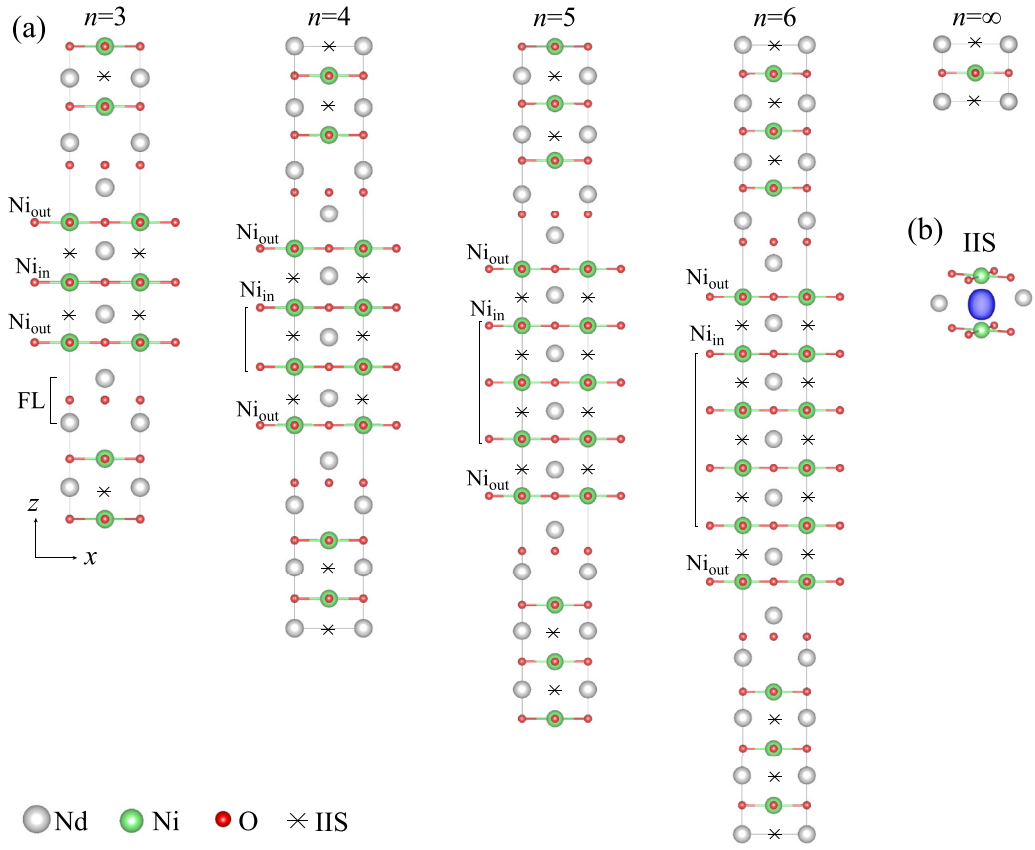

FIG. 5. (a) Crystal structures for $Nd_{n+1}Ni_nO_{2n+2}$ ($n = 3 - 6$ and ∞). Nonequivalent Ni atoms (Ni_{in} and Ni_{out}) are labeled. (b) IIS orbital (blue) located at the AOV site.

and the I_{OP} of $Nd_{n+1}Ni_nO_{2n+2}H_x$. As depicted in Fig. 1(c), the L_{3d-IIS}, which is directly related to the ratio of hopping strength (t_{3d-IIS}) and energy difference (Δ_{3d-IIS}), varies significantly with x. Due to the symmetric restriction, intracell hopping between the $3d_{x2-y2}$ orbital and other orbitals around E_F (including the Ni d_{z2} orbital, Nd $5d$ orbitals, and IIS) is negligible, except for the sizable hopping with O $p\sigma$ (defined as t_1). Meanwhile, the intracell hopping between IIS orbital and O $p\sigma$ (defined as t_2) is large, giving rise to substantial out of plane indirect intercell hopping between $3d_{x2-y2}$ and IIS via O $p\sigma$ (defined as t_{3d-IIS}). For $Nd_{n+1}Ni_nO_{2n+2}$ without H intercalation, as illustrated in Fig. 4(a), the Ni_{in} $3d_{x2-y2}$ orbital hybridizes with eight next nearest neighbor (NNN) IIS orbitals along the (1 0 0), (–1 0 0), (0 1 0), and (0 −1 0) directions. On the other hand, the Ni_{out} atom has one neighboring NiO_2 plane, and can couple with four NNN IIS orbitals. Interestingly, the calculated t_{3d-IIS} obtained through Wannier downfolding is approximately −0.21 eV for all cases, independent of n and x. Therefore, the total hopping strength between $3d_{x2-y2}$ and IIS in $Nd_{n+1}Ni_nO_{2n+2}$ is proportional to the number of NNN IIS orbitals. Consequently, the average hopping strength ($\bar{t}_{3d-IIS}$) per Ni $3d_{x2-y2}$ orbital can be estimated by dividing the total hopping strength by the total number of Ni atoms: $\bar{t}_{3d-IIS} = [8 \times (n-2) + 4 \times 2]/n\, t_{3d-IIS} = (8n-8)/n\, t_{3d-IIS}$. For $n = \infty$, $\bar{t}_{3d-IIS}$ is 8 t_{3d-IIS}, and for $n = 5$, $\bar{t}_{3d-IIS}$ is reduced to 6.4 t_{3d-IIS}.

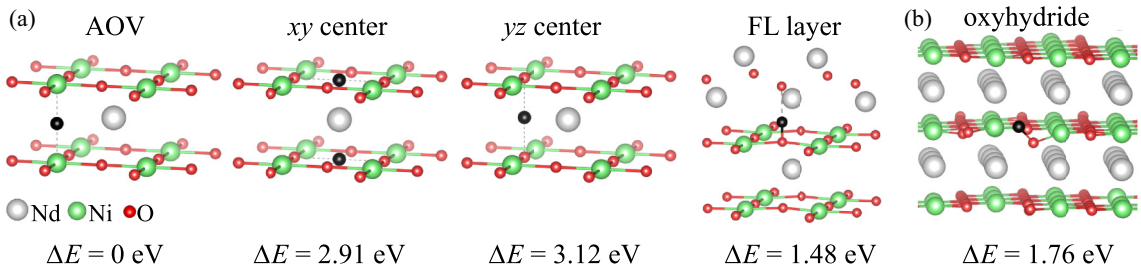

FIG. 6. (a) Four possible high-symmetry H configurations in $Nd_6Ni_5O_{12}$, i.e., AOV site, the center of the xy plane, the center of the yz plane, and the site in the FL layer. (b) Relaxed crystal structure of the oxyhydride configuration. Energy differences for these configurations are listed below each configuration. The total energy of the H occupying the AOV site is set to zero.

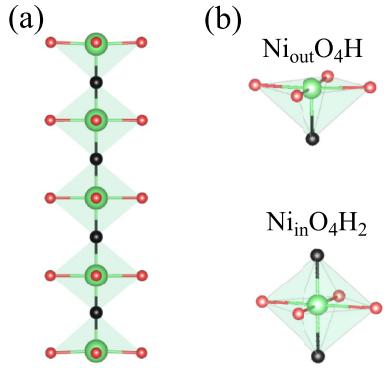

FIG. 7. (a) Local environment of one H chain in $Nd_6Ni_5O_{12}$. (b) The local environment of H-inserted Ni atoms.

When H atoms occupy the AOV sites, the number of NNN hopping $t_{3d-\mathrm{IIS}}$ for both Ni_{out} and Ni_{in} atoms decreases significantly. In general, the insertion of one H atom results in the annihilation of eight $t_{3d-\mathrm{IIS}}$ in $Nd_{n+1}Ni_nO_{2n+2}$, while the remaining $t_{3d-\mathrm{IIS}}$ without H remains unaffected. Consequently, the $\bar{t}_{3d-\mathrm{IIS}}$ is weakened due to the reduction of the total number of NNN IIS orbitals. Meanwhile, the variation in the energy difference ($\Delta_{3d-\mathrm{IIS}}$) is within a range of 8% for different values of n and x. Specifically, for different values of x, the $\Delta_{3d-\mathrm{IIS}}$ changes from 3.21 to 3.27 for $n = 3$, and from 3.01 to 3.10 for $n = \infty$. Therefore, the orbital hybridization $L_{3d-\mathrm{IIS}}$ remains predominantly proportional to $\bar{t}_{3d-\mathrm{IIS}}$ for the H-intercalated systems. The decrease in $\bar{t}_{3d-\mathrm{IIS}}$ results in a more 2D electronic structure.

Combining the above discussions on I_{OP} and $\bar{t}_{3d-\mathrm{IIS}}$, we depict their values in Fig. 4(b) (also see Table II in the Appendix). For a selected n, five different x are considered ($x = 0$, 0.25, 0.5, 0.75, 1). Obviously, for a given n, both $\bar{t}_{3d-\mathrm{IIS}}$ and I_{OP} decrease with decreasing x. Furthermore, for a given x, the $\bar{t}_{3d-\mathrm{IIS}}$ decreases while the I_{OP} increases as n decreases. Based on the superconducting x range obtained in the $n = \infty$ system [47] [as labeled by "*" in Fig. 4(b)], the maximum $\bar{t}_{3d-\mathrm{IIS}}$ ($\bar{t}_{\max}$) and $I_{\min}$ for infinite nickelate can be determined (black dashed lines). Clearly, a system with smaller n enables a larger region of H doping where both small $L_{3d-\mathrm{IIS}}$ and large I_{OP} remain, which corresponds to the quasi-2D electronic structure. Because it is difficult to prepare SPNs with larger n experimentally, values for larger n ($n > 6$) compounds are not calculated, leading to a gap between the lines for $n = \infty$ and $n = 3 - 6$ in Fig. 4(b).

IV. DISCUSSION AND SUMMARY

The intriguing feature of $Nd_{n+1}Ni_nO_{2n+2}H_{(n-1)x}$ with smaller n lies in the larger hydrogen region, where small orbital hybridization and large orbital polarization are maintained. This feature may benefit the superconductivity of SPNs when applying the concept of "orbital distillation" effect proposed in cuprates [53,70]. The term orbital distillation in cuprates refers to purifying the $3d_{x2-y2}$ property of the CuO_2 plane. In the case of SPNs, purifying the $3d_{x2-y2}$ mainly involves reducing the hybridization between the $3d_{x2-y2}$ and the $3d_{z2}$ and IIS orbitals. By adopting the critical $\bar{t}_{\max}$ and $I_{\min}$ in (Nd,Sr)NiO_2, the x range possessing quasi-2D $3d_{x2-y2}$ increases as the value of n decreases in the SPNs, as depicted in Fig. 4(b). For $n = \infty$, this range is very narrow, approximately 0.22–0.28. It greatly expands to 0.03–0.63 for $n = 5$. In other words, the superconductivity may be less sensitive to the H doping for SPNs with smaller n. This implies that it might be more attainable to achieve superconductivity in a system with a smaller value of n. It has to be emphasized that, as the direct link between electronic structure and superconductivity is still unclear, further investigation is necessary to determine the influence of the number of layers and H intercalation on superconductivity. Additionally, more in-depth exploration, considering the many-body effect [71,81], is needed to explain the observed superconductivity in H-inserted nickelates.

It is important to note that the coupling between interlayer d_{z2} orbitals may be taken into consideration when H is intercalated, as they become partially filled. Interestingly, the significant indirect hopping strength between d_{z2} states via H s orbitals (0.85 eV) (Fig. 14 in the Appendix) needs to be incorporated when constructing the model Hamiltonian for $Nd_{n+1}Ni_nO_{2n-1}H_{(n-1)x}$ ($x > 0$). Furthermore, except for the consideration of H, the occupation of Ni $3d^{9-\delta}$ ($\delta = 1/n$) is another important factor that needs to be considered in understanding the superconductivity of $Nd_{n+1}Ni_nO_{2n-1}H_{(n-1)x}$. To achieve superconductivity, it is likely necessary to regulate the filling of the $3d$ orbital through hole or electron doping for systems with larger or smaller values of n. As for the $n = 3$ case, although superconductivity can occur in a very large H concentration regime, the lower $3d$ filling orbital may hinder the superconductivity [11].

In summary, the intercalation of H in square-planar nickelates $Nd_{n+1}Ni_nO_{2n+2}$ is investigated by first-principles calculations. H atoms tend to form separated 1D chains along the c axis because of the existence of fluorite layers. The insertion of H leads to the annihilation of IIS orbitals, which reduces the out of plane hybridization of $3d_{x2-y2}$ orbitals. Meanwhile, the strong hybridization between Ni $3d_{z2}$ and H $1s$

TABLE I. Binding energies of H located at AOV sites in $Nd_{n+1}Ni_nO_{2n+2}H_{(n-1)x}$ ($n = 3 - 6$, and ∞, $x = 0.25$, 0.5, 0.75, 1) calculated by the chemical potential of H atom (E_{bH}) and 1/2 H_2 (E_{bH2}).

x	0.25		0.5		0.75		1	
E_b (eV)	E_{bH}	E_{bH2}	E_{bH}	E_{bH2}	E_{bH}	E_{bH2}	E_{bH}	E_{bH2}
$Nd_4Ni_3O_8H_{2x}$	–3.15	0.16	–3.09	0.22	–3.06	0.25	–3.02	0.29
$Nd_5Ni_4O_{10}H_{3x}$	–3.34	–0.03	–3.33	–0.02	–3.26	0.05	–3.22	0.09
$Nd_6Ni_5O_{12}H_{4x}$	–3.38	–0.07	–3.37	–0.06	–3.30	0.01	–3.27	0.04
$Nd_7Ni_6O_{14}H_{5x}$	–3.41	–0.10	–3.40	–0.09	–3.33	–0.02	–3.29	0.02
$NdNiO_2H_x$	–3.59	–0.28	–3.57	–0.26	–3.55	–0.24	–3.52	–0.21

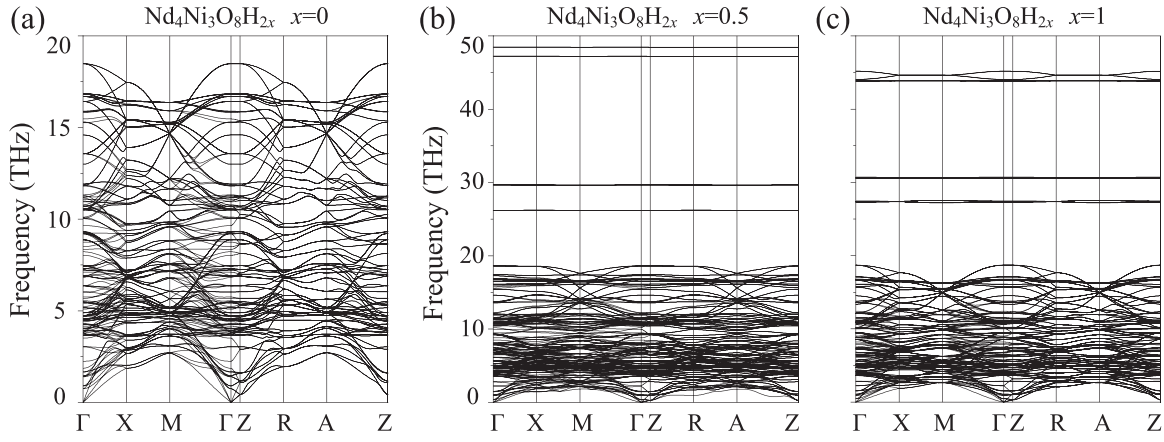

FIG. 8. Phonon spectra of $\sqrt{2} \times \sqrt{2} \times 1$ $Nd_4Ni_3O_8$ supercell doped with (a) $x = 0$, (b) $x = 0.5$, (c) $x = 1$.

decreases the orbital polarization. The combination of weaker orbital hybridization and stronger orbital polarization results in a more 2D-like behavior for SPNs with smaller n values, which may suggest a reduced sensitivity to H in terms of superconductivity.

ACKNOWLEDGMENTS

This work is supported by the Fundamental Research Funds for the Central Universities (buctrc202402), the National Key Research and Development of China (Grant No. 2022YFA1402401), NSFC (Grant No. 12088101), and NSAF (Grant No. U2230402). L.Q. acknowledges the support by NSFC (Grants No. 12274061, No. 52072059, and No. 11774044) and the Science and Technology Department of Sichuan Province (Grants No. 2021JDJQ0015 and No. 2022ZYD0014). Computations are done at the Tianhe-JK supercomputer at CSRC.

APPENDIX

Without loss of generality, five systems are investigated, with the crystal structures depicted in Fig. 5. Taking the $2 \times 2 \times 1$ supercell of $Nd_6Ni_5O_{12}$ as an example, four possible high-symmetry H positions, i.e., AOV position, the center of the xy plane, the center of the yz plane, and the site in FL are considered, as given in Fig. 6(a). The energy differences for each configuration are listed below. Clearly, the configuration with intercalated hydrogen atoms occupying AOV sites exhibits the lowest energy, while the other configurations display significantly higher energies. Moreover, the test hydrogen atom is positioned in a random and low-symmetry location. After full structure relaxations, hydrogen ion either bonds with oxygen to form a metastable oxyhydride configuration (when the initial H is positioned near O) or moves automatically to the AOV site (when the initial H is positioned near AOV). The relaxed structure of the oxyhydride configuration is shown in Fig. 6(b), with a total energy 1.76 eV higher than the ground state. Therefore, after a sufficiently long relaxation time, H atoms in the oxyhydride site could move to the AOV site to reduce the total energy.

From Fig. 7(a), the existence of FL blocks the H chains in $Nd_6Ni_5O_{12}H_{4x}$, and four H atoms form one H chain, different from the case in $NdNiO_2$. This gives rise to two local environments of Ni atoms, namely, $Ni_{out}O_4H$ and $Ni_{in}O_4H_2$, as illustrated in Fig. 7(b).

The binding energy (E_b) is calculated to investigate whether it is energetically favorable to intercalate the H atoms,

$$E_b = E[Nd_{n+1}Ni_nO_{2n+2}H_{(n-1)x}] - E[Nd_{n+1}Ni_nO_{2n+2}] - (n-1)x(\mu[H]), \quad \text{(A1)}$$

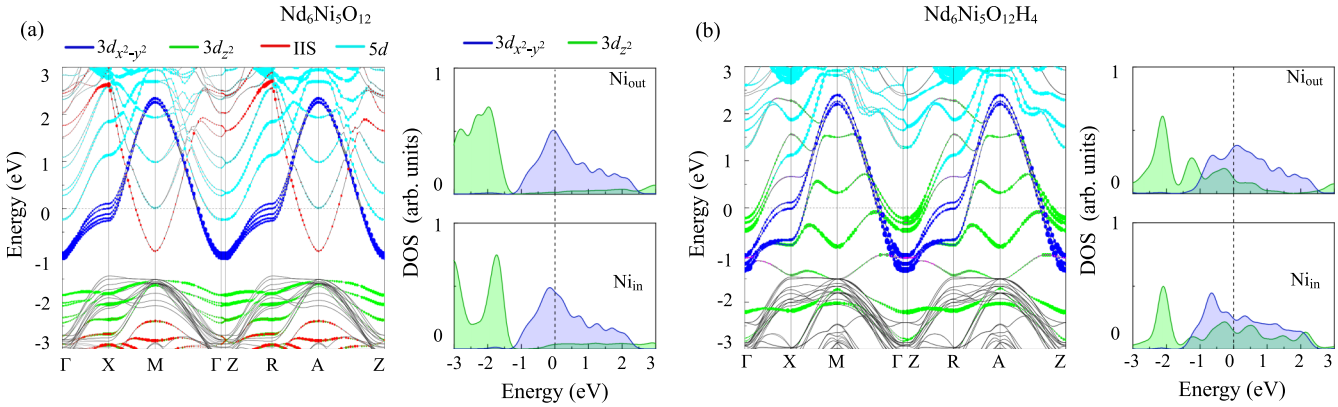

FIG. 9. Fully projected band structures (left panel) and DOS (right panel) for (a) $Nd_6Ni_5O_{12}$ and (b) $Nd_6Ni_5O_{12}H_4$. DOS for nonequivalent Ni_{out} and Ni_{in} are given separately.

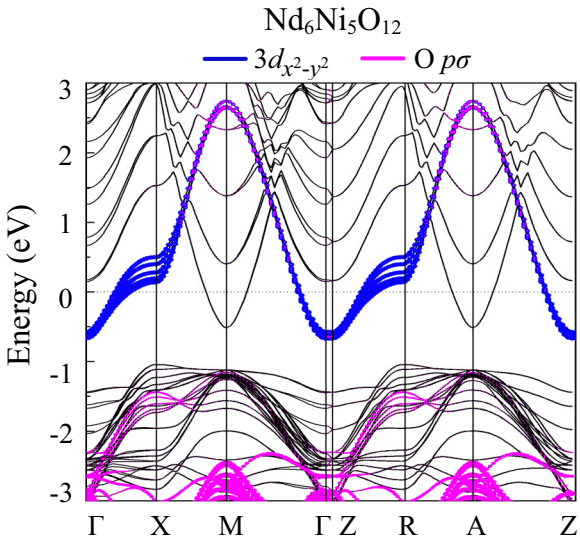

FIG. 10. Band structure for $Nd_6Ni_5O_{12}$ with Ni $3d_{x2-y2}$ and O $p\sigma$ orbitals projected.

where $E[Nd_{n+1}Ni_nO_{2n+2}]$ and $E[Nd_{n+1}Ni_nO_{2n+2}H_{(n-1)x}]$ are the total energies of $Nd_{n+1}Ni_nO_{2n+2}$ and $Nd_{n+1}Ni_nO_{2n+2}H_{(n-1)x}$, respectively. The chemical potential of H, denoted as μ[H], is likely to fall between the H-poor (μ[H] of an isolated H atom) and H-rich (μ[H] of the H_2 molecule) condition.

The E_b values are given in Table I, and E_{bH} and E_{bH2} are the formation energies calculated by the chemical potential of the H atom and H_2 molecule. Here, the more negative the value, the more energetically favorable to form $Nd_{n+1}Ni_nO_{2n+2}H_{(n-1)x}$. For $NdNiO_2H_x$, both E_{bH} and E_{bH2} are negative, indicating that the incorporation of H is energetically favorable. As n decreases, E_b generally increases. The comparable values of E_b indicate the possibility of H insertion in square-planer nickelate. For example, the calculated E_b for $NdNiO_2H_{0.25}$ ranges from -3.59 to -0.28 eV, and for $Nd_6Ni_5O_{12}H$, it ranges from -3.38 to -0.07 eV. The E_{bH} for all n and x is always negative, while E_{bH2} is positive for small n. The values of E_{bH} and E_{bH2} increase with x, suggesting that a higher concentration of H is less energetically favorable. Therefore, as n increases and x decreases, the incorporation of H becomes more energetically favorable.

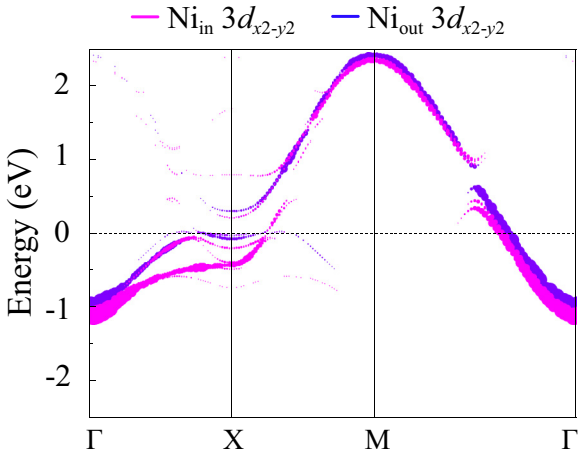

FIG. 11. The band structure of $Nd_6Ni_5O_{12}H_{0.5}$, with $3d_{x2-y2}$ orbital projected onto the Ni_{Ni} and Ni_{out} atoms.

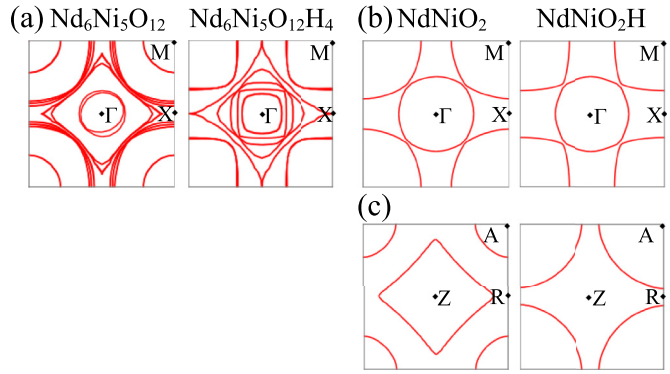

FIG. 12. Fermi Surfaces for (a) $Nd_6Ni_5O_{12}$ (left panel) and (b) $Nd_6Ni_5O_{12}H_4$ (right panel) in the $k_z = 0$ section. Panel (c) is the same as (b) but for the $k_z = \pi$ section.

Phonon spectra are calculated to compare properties across different hydrogen concentrations. Due to the large cell of $Nd_{n+1}Ni_nO_{2n+2}H_{(n-1)x}$, phonon calculations are performed for $Nd_4Ni_3O_8H_{2x}$ ($x = 0$, 0.5, and 1) with supercell $\sqrt{2} \times \sqrt{2} \times 1$, as depicted in Fig. 8. Considering the structural resemblance, we can expect similar variation trends for hydrogen intercalation across different n systems. Clearly, all the phonon frequencies are positive, indicating the dynamical stability of these systems. The phonon dispersions between 0 and 20 THz are almost the same with different x. Meanwhile, additional phonon modes from light H atoms are visible at frequencies between 26 and 49 THz. The vibration modes around $\sim$ 46 THz ($\sim$ 30 THz) are contributed by the out of plane (in-plane) vibrations, similar to the situations in H-doped infinite nickelate [49]. The presence of localized phonon dispersion with high frequencies provides methods for detecting hydrogen in SPNs, such as phonon measurements through RIXS and inelastic neutron scattering spectra [73].

The band structure for square-planar $Nd_{n+1}Ni_nO_{2n+2}$ with $n = 5$ is given in Fig. 9(a). The existence of FL blocks the c-axis interaction, leading to remarkable similar band dispersions between $k_z = 0$ (Γ–X–M–Γ) and $k_z = \pi$ (Z-R-A-Z)

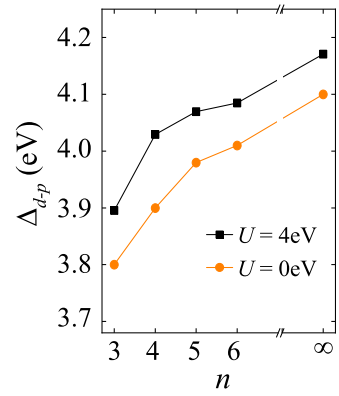

FIG. 13. Charge-transfer energy Δ_{d-p} versus n for $x = 0.0$. The black and orange lines are results obtained by DFT+U and DFT methods, respectively.

TABLE II. The source data of $2 \times 2 \times 1$ supercell $Nd_6Ni_5O_{12}H_{4x}$ for calculating the I_{OP} and $\bar{t}_{3d-IIS}$.

x	n_{3dz2}	$n_{3dx2-y2}$	I_{OP}	t_{3d-IIS}	n_{Ni}	$\bar{t}_{3d-IIS}$
0	1.711	1.133	0.203	256	40	6.4
0.25	1.672	1.156	0.182	192	40	4.8
0.5	1.637	1.176	0.164	128	40	3.2
0.75	1.590	1.18	10.148	64	40	1.6
1	1.556	1.20	0.129	0	40	0

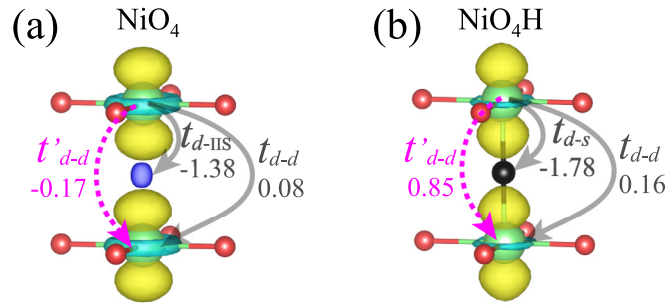

FIG. 14. The hopping paths and the corresponding strength (in units of eV) for interlayer coupling between d_{z2} orbitals. (a) Local environment of NiO_4. (b) Local environment of NiO_4H. The direct hopping paths (t_{d-IIS}, t_{d-s}, and t_{d-d}) are labeled by gray lines, and the indirect hopping paths (t'_{d-d}) are labeled as dashed pink lines.

plane in finite nickelates, which is also reflected in the flat dispersion of $3d_{z2}$ along the Γ-Z line. Moreover, the reduced proportion of Nd d orbitals around E_F in finite-layer nickelates indicates the more quasi-2D characteristics compared to the $n = \infty$ case. In addition, the existence of FL separates Ni atoms into nonequivalent Ni_{out} and Ni_{in} atoms. From the projected DOS in Fig. 9(a), the distribution of $3d_{x2-y2}$ orbitals is similar for both Ni atoms. Meanwhile, with a small proportion around E_F, the $3d_{z2}$ orbitals distribute much differently below -2 eV, which can be explained by the molecular subband picture induced by the quantum confinement along the c axis [42,66]. For the H-inserted case [Fig. 9(b)], the band dispersions for $k_z = 0$ (Γ-X-M-Γ) and $k_z = \pi$ (Z-R-A-Z) planes remain very close. However, the difference between the two nonequivalent Ni atoms becomes more pronounced. The occupation of the Ni_{in} d_{z2} orbital decreases more dramatically compared to that of Ni_{out}. The Ni_{out} atom bonds with one H atom, forming a $Ni_{out}O_4H$ local environment, while the Ni_{in} atom bonds with two H atoms, forming $Ni_{in}O_4H_2$ [Fig. 7(b)]. The stronger hybridization between the H $1s$ orbital and Ni_{in} $3d_{z2}$ lifts up the antibonding state closer to E_F. Because the total $3d$ filling remains almost unchanged, the downward energy shift of the $3d_{x2-y2}$ orbital is more pronounced for the Ni_{in} atom compared to the Ni_{out} atom. The projected band structure for $Nd_6Ni_5O_{12}$ is illustrated in Fig. 10, where the $3d_{x2-y2}$ orbitals of both Ni_{in} and Ni_{out} are coupled with the O $p\sigma$ orbitals. The band structure of $Nd_6Ni_5O_{12}H_{0.5}$ is depicted in Fig. 11, indicating a smaller downshift in the $3d_{x2-y2}$ orbital of Ni_{out} compared to that of Ni_{in}.

Due to the comparable band dispersions observed in the $k_z = 0$ and $k_z = \pi$ sections of finite nickelates, Fig. 12 displays the Fermi surface (FS) specifically for the $k_z = 0$ section. For $n = 5$ upon H insertion, the upward shift of the d_{z2} orbital results in an increased number of electron pockets around the Γ point. Meanwhile, the downward shift of d_{x2-y2} changes the shape of the FS sheets. For $n = \infty$, the FSs are given for both $k_z = 0$ and $k_z = \pi$. Upon H insertion, FS undergoes very slight changes for the $k_z = 0$ section, while the electron pocket around A vanishes for the $k_z = \pi$ section.

The Δ_{d-p} values presented in Fig. 3(d) are obtained using the DFT+U method. These values should be obtained using the DFT method to make comparisons to U. However, we have to emphasize that the consideration of Coulomb correlations U has a slight influence on these Δ_{d-p} values. Taking the cases under $x = 0.0$ as an example, as illustrated in Fig. 13, the differences between Δ_{d-p} values obtained with and without U are approximately ~ 0.1 eV.

Taking the case of $n = 5$ as an example, the source data required to calculate the orbital polarization I_{OP} [$I_{OP} = (n_{3dz2}-n_{3dx2-y2})/(n_{3dz2}+n_{3dx2-y2})$] are provided in Table II. The averaged hopping strength $\bar{t}_{3d-IIS}$ can be estimated by dividing the total number of hopping paths between $3d_{x2-y2}$ and IIS by the total number of Ni atoms, as given in Table II.

The interlayer hopping has to be considered since the d_{z2} state becomes partially filled when H is intercalated. Taking $Nd_6Ni_5O_{12}H_2$ as an example, for both local NiO_4 and NiO_4H environments, the hopping paths are illustrated in Fig. 14, including direct hopping (t_{d-IIS}: $d_{z2} \rightarrow$ IIS, t_{d-s}: $d_{z2} \rightarrow$ H$-s$, t_{d-d}: $d_{z2} \rightarrow d_{z2}$) and indirect hopping ($t'_{d-d}$: $d_{z2} \rightarrow d_{z2}$). The corresponding hopping strengths are also provided. In Fig. 14, it can be observed that the direct couplings between $d_{z2} \rightarrow$ IIS ($t_{d-IIS} = -1.38$ eV) and $d_{z2} \rightarrow$ H$-s$ ($t_{d-s} = -1.78$ eV) are significant, and the indirect interlayer coupling between d_{z2} orbitals through H-s ($t'_{d-d} = 0.85$ eV) is large. However, the direct coupling of $d_{z2} \rightarrow d_{z2}$ (t_{d-d}) is small in both cases, with values being 0.08 and 0.16 eV for cases without and with H bonding, respectively.

[1] M. Greenblatt, Ruddlesden-Popper $Ln_{n+1}Ni_nO_{3n+1}$ nickelates: Structure and properties, Curr. Opin. Solid State Mater. Sci. **2**, 174 (1997).

[2] Q. Li, C. P. He, X. Y. Zhu, J. Si, X. W. Fan, and H.-H. Wen, Contrasting physical properties of the trilayer nickelates $Nd_4Ni_3O_{10}$ and $Nd_4Ni_3O_8$, Sci. China: Phys., Mech. Astron. **64**, 227411 (2020).

[3] V. V. Poltavets, K. A. Loshkin, T. Egami, and M. Greenblatt, The oxygen deficient Ruddlesden-Popper $La_3Ni_2O_{7-\delta}$ ($\delta = 0.65$) phase: Structure and properties, Mater. Res. Bull. **41**, 955 (2006).

[4] J. Zhang, A. S. Botana, J. W. Freeland, D. Phelan, H. Zheng, V. Pardo, M. R. Norman, and J. F. Mitchell, Large orbital polarization in a metallic square-planar nickelate, Nat. Phys. **13**, 864 (2017).

[5] P. Hansmann, X. Yang, A. Toschi, G. Khaliullin, O. K. Andersen, and K. Held, Turning a nickelate Fermi surface into a cupratelike one through

heterostructuring, Phys. Rev. Lett. **103**, 016401 (2009).

[6] D. Li, K. Lee, B. Y. Wang, M. Osada, S. Crossley, H. R. Lee, Y. Cui, Y. Hikita, and H. Y. Hwang, Superconductivity in an infinite-layer nickelate, Nature (London) **572**, 624 (2019).

[7] D. Li, B. Y. Wang, K. Lee, S. P. Harvey, M. Osada, B. H. Goodge, L. F. Kourkoutis, and H. Y. Hwang, Superconducting dome in $Nd_{1-x}Sr_xNiO_2$ infinite layer films, Phys. Rev. Lett. **125**, 027001 (2020).

[8] S. Zeng, C. S. Tang, X. Yin, C. Li, M. Li, Z. Huang, J. Hu, W. Liu, G. J. Omar, H. Jani, Z. S. Lim, K. Han, D. Wan, P. Yang, S. J. Pennycook, A. T. S. Wee, and A. Ariando, Phase diagram and superconducting dome of infinite-layer $Nd_{1-x}Sr_xNiO_2$ thin films, Phys. Rev. Lett. **125**, 147003 (2020).

[9] M. Osada, B. Y. Wang, B. H. Goodge, K. Lee, H. Yoon, K. Sakuma, D. Li, M. Miura, L. F. Kourkoutis, and H. Y. Hwang, A superconducting praseodymium nickelate with infinite layer structure, Nano Lett. **20**, 5735 (2020).

[10] M. Osada, B. Y. Wang, B. H. Goodge, S. P. Harvey, K. Lee, D. Li, L. F. Kourkoutis, and H. Y. Hwang, Nickelate superconductivity without rare-earth magnetism: $(La, Sr)NiO_2$, Adv. Mater. **33**, 45 (2021).

[11] G. A. Pan, D. F. Segedin, H. LaBollita, Q. Song, E. M. Nica, B. H. Goodge, A. T. Pierce, S. Doyle, S. Novakov, D. C. Carrizales, A. T. N'Diaye, P. Shafer, H. Paik, J. T. Heron, J. A. Mason, A. Yacoby, L. F. Kourkoutis, O. Erten, C. M. Brooks, A. S. Botana *et al.*, Superconductivity in a quintuple-layer square-planar nickelate, Nat. Mater. **21**, 160 (2022).

[12] H. LaBollita and A. S. Botana, Correlated electronic structure of a quintuple-layer nickelate, Phys. Rev. B **105**, 085118 (2022).

[13] H. LaBollita, M.-C. Jung, and A. S. Botana, Many-body electronic structure of $d^{9-\delta}$ layered nickelates, Phys. Rev. B **106**, 115132 (2022).

[14] H. Li, P. Hao, J. Zhang, K. Gordon, A. G. Linn, X. Chen, H. Zheng, X. Zhou, J. F. Mitchell, and D. S. Dessau, Electronic structure and correlations in planar trilayer nickelate $Pr_4Ni_3O_8$, Sci. Adv. **9**, eade4418 (2023).

[15] D. F. Segedin, B. H. Goodge, G. A. Pan, Q. Song, H. LaBollita, M.-C. Jung, H. E.-Sherif, S. Doyle, A. Turkiewicz, N. K. Taylor, J. A. Mason, A. T. N'Diaye, H. Paik, I. E. Baggari, A. S. Botana, L. F. Kourkoutis, C. M. Brooks, and J. A. Mundy, Limits to the strain engineering of layered square-planar nickelate thin films, Nat. Commun. **14**, 1468 (2023).

[16] Q. Gu, Y. Li, S. Wan, H. Li, W. Guo, H. Yang, Q. Li, X. Zhu, X. Pan, Y. Nie, and H.-H. Wen, Single particle tunneling spectrum of superconducting $Nd_{1-x}Sr_xNiO_2$ thin films, Nat. Commum. **11**, 6027 (2020).

[17] Y. Gu, S. Zhu, X. Wang, J. Hu, and H. Chen, A substantial hybridization between correlated Ni-d orbital and itinerant electrons in infinite-layer nickelates, Commun. Phys. **3**, 84 (2020).

[18] Z. Wang, G.-M. Zhang, Y. Yang, and F.-C. Zhang, Distinct pairing symmetries of superconductivity in infinite-layer nickelates, Phys. Rev. B **102**, 220501(R) (2020).

[19] K.-W. Lee and W. E. Pickett, Infinite-layer $LaNiO_2$: Ni^{1+} is not Cu^{2+}, Phys. Rev. B **70**, 165109 (2004).

[20] C. Chen, R. Ma, X. Sui, Y. Liang, B. Huang, and T. Ma, Antiferromagnetic fluctuations and dominant d_{xy}-wave pairing symmetry in nickelate-based superconductors, Phys. Rev. B **106**, 195112 (2022).

[21] M. Jiang, M. Berciu, and G. A. Sawatzky, Critical nature of the Ni spin state in doped $NdNiO_2$, Phys. Rev. Lett. **124**, 207004 (2020).

[22] F. Lechermann, Late transition metal oxides with infinite-layer structure: Nickelates versus cuprates, Phys. Rev. B **101**, 081110(R) (2020).

[23] Y.-H. Zhang and A. Vishwanath, Type-II t-J model in superconducting nickelate $Nd_{1-x}Sr_xNiO_2$, Phys. Rev. Res. **2**, 023112 (2020).

[24] P. Jiang, L. Si, Z. Liao, and Z. Zhong, Electronic structure of rare-earth infinite-layer $RNiO_2$ (R = La, Nd), Phys. Rev. B **100**, 201106(R) (2019).

[25] V. I. Anisimov, D. Bukhvalov, and T. M. Rice, Electronic structure of possible nickelate analogs to the cuprates, Phys. Rev. B **59**, 7901 (1999).

[26] A. S. Botana, V. Pardo, and M. R. Norman, Electron doped layered nickelates: Spanning the phase diagram of the cuprates, Phys. Rev. Mater. **1**, 021801(R) (2017).

[27] A. S. Botana and M. R. Norman, Similarities and differences between $LaNiO_2$ and $CaCuO_2$ and implications for superconductivity, Phys. Rev. X **10**, 011024 (2020).

[28] M. Kitatani, L. Si, O. Janson, R. Arita, Z. Zhong, and K. Held, Nickelate superconductors—a renaissance of the one-band Hubbard model, npj Quantum Mater. **5**, 59 (2020).

[29] P. Werner and S. Hoshino, Nickelate superconductors: Multiorbital nature and spin freezing, Phys. Rev. B **101**, 041104(R) (2020).

[30] V. M. Katukuri, N. A. Bogdanov, O. Weser, J. van den Brink, and A. Alavi, Electronic correlations and magnetic interactions in infinite-layer $NdNiO_2$, Phys. Rev. B **102**, 241112(R) (2020).

[31] F. Lechermann, Emergent flat-band physics in $d^{9-\delta}$ multilayer nickelates, Phys. Rev. B **105**, 155109 (2022).

[32] M. Hepting, D. Li, C. J. Jia, H. Lu, E. Paris, Y. Tseng, X. Feng, M. Osada, E. Been, Y. Hikita, Y.-D. Chuang, Z. Hussain, K. J. Zhou, A. Nag, M. Garcia-Fernandez, M. Rossi, H. Y. Huang, D. J. Huang, Z. X. Shen, T. Schmitt *et al.*, Electronic structure of the parent compound of superconducting infinite-layer nickelates, Nat. Mater. **19**, 381 (2020).

[33] H. Sakakibara, H. Usui, K. Suzuki, T. Kotani, H. Aoki, and K. Kuroki, Model construction and a possibility of cupratelike pairing in a new d^9 nickelate superconductor $(Nd, Sr)NiO_2$, Phys. Rev. Lett. **125**, 077003 (2020).

[34] X. Wu, D. D. Sante, T. Schwemmer, W. Hanke, H. Y. Hwang, S. Raghu, and R. Thomale, Robust d_{x2-y2}-wave superconductivity of infinite-layer nickelates, Phys. Rev. B **101**, 060504(R) (2020).

[35] H. Zhang, L. Jin, S. Wang, B. Xi, X. Shi, F. Ye, and J.-W. Mei, Effective Hamiltonian for nickelate oxides $Nd_{1-x}Sr_xNiO_2$, Phys. Rev. Res. **2**, 013214 (2020).

[36] G.-M. Zhang, Y.-f. Yang, and F.-C. Zhang, Self-doped Mott insulator for parent compounds of nickelate superconductors, Phys. Rev. B **101**, 020501(R) (2020).

[37] M. Crespin, P. Levitz, and L. Gatineau, Reduced forms of $LaNiO_3$ perovskite. Part 1—evidence for new phases: $La_2Ni_2O_5$ and $LaNiO_2$, J. Chem. Soc., Faraday Trans. **279**, 1181 (1983).

[38] M. A. Hayward, M. A. Green, M. J. Rosseinsky, and J. Sloan, Sodium hydride as a powerful reducing agent for topotactic oxide deintercalation: Synthesis and characterization of the nickel(I) oxide $LaNiO_2$, J. Am. Chem. Soc. **121**, 8843 (1999).

[39] Q. Gao, Y. Zhao, X.-J. Zhou, and Z. Zhu, Preparation of superconducting thin films of infinite-layer nickelate $Nd_{0.8}Sr_{0.2}NiO_2$, Chin. Phys. Lett. **38**, 077401 (2021).

[40] K. Lee, B. H. Goodge, D. Li, M. Osada, B. Y. Wang, Y. Cui, L. F. Kourkoutis, and H. Y. Hwang, Aspects of the synthesis of thin film superconducting infinite-layer nickelates, APL Mater. **8**, 041107 (2020).

[41] B.-X. Wang, H. Zheng, E. Krivyakina, O. Chmaissem, P. Papa Lopes, J. W. Lynn, L. C. Gallington, Y. Ren, S. Rosenkranz, J. F. Mitchell, and D. Phelan, Synthesis and characterization of bulk $Nd_{1-x}Sr_xNiO_2$ and $Nd_{1-x}Sr_xNiO_3$, Phys. Rev. Mater. **4**, 084409 (2020).

[42] M.-C. Jung, J. Kapeghian, C. Hanson, B. Pamuk, and A. S. Botana, Electronic structure of higher-order Ruddlesden-Popper nickelates, Phys. Rev. B **105**, 085150 (2022).

[43] G. A. Pan, Q. Song, D. F. Segedin, M.-C. Jung, H. E.-Sherif, E. E. Fleck, B. H. Goodge, S. Doyle, D. C. Carrizales, A. T. N'Diaye, P. Shafer, H. Paik, L. F. Kourkoutis, I. E. Baggari, A. S. Botana, C. M. Brooks, and J. A. Mundy, Synthesis and electronic properties of $Nd_{n+1}Ni_nO_{3n+1}$ Ruddlesden-Popper nickelate thin films, Phys. Rev. Mater. **6**, 055003 (2022).

[44] L. Si, W. Xiao, J. Kaufmann, J. M. Tomczak, Y. Lu, Z. Zhong, and K. Held, Topotactic hydrogen in nickelate superconductors and akin infinite-layer oxides ABO_2, Phys. Rev. Lett. **124**, 166402 (2020).

[45] O. I. Malyi, J. Varignon, and A. Zunger, Bulk $NdNiO_2$ is thermodynamically unstable with respect to decomposition while hydrogenation reduces the instability and transforms it from metal to insulator, Phys. Rev. B. **105**, 014106 (2022).

[46] C. Qin, M. Jiang, and L. Si, Effects of different concentrations of topotactic hydrogen impurities on the electronic structure of nickelate superconductors, arXiv:2307.12020.

[47] X. Ding, C. C. Tam, X. Sui, Y. Zhao, M. Xu, J. Choi, H. Leng, Ji. Zhang, M. Wu, H. Xiao, X. Zu, M. Garcia-Fernandez, S. Agrestini, X. Wu, Q. Wang, P. Gao, S. Li, B. Huang, K.-J. Zhou, and L. Qiao, Critical role of hydrogen for superconductivity in nickelates, Nature (London) **615**, 50 (2023).

[48] L. Si, P. Worm, D. Chen, and K. Held, Topotactic hydrogen forms chains in ABO_2 nickelate superconductors, Phys. Rev. B **107**, 165116 (2023).

[49] L. Si, P. Worm, and K. Held, Fingerprints of topotactic hydrogen in nickelate superconductors, Crystals **12**, 656 (2022).

[50] M. Hirayama, S. Matsuishi, H. Hosono, and S. Murakami, Electrides as a new platform of topological materials, Phys. Rev. X **8**, 031067 (2018).

[51] S. Matsuishi, Y. Toda, M. Miyakawa, K. Hayashi, T. Kamiya, M. Hirano, I. Tanaka, and H. Hosono, High-density electron anions in a nanoporous single crystal: $[Ca_{24}Al_{28}O_{64}]^{4+}(4e^-)$, Science **301**, 626 (2003).

[52] C. Weber, C. Yee, K. Haule, and G. Kotliar, Scaling of the transition temperature of hole-doped cuprate superconductors with the charge-transfer energy, Europhys. Lett. **100**, 37001 (2012).

[53] H. Sakakibara, H. Usui, K. Kuroki, R. Arita, and H. Aoki, Origin of the material dependence of T_c in the single layered cuprates, Phys. Rev. B **85**, 064501 (2012).

[54] E. Pavarini, I. Dasgupta, T. Saha-Dasgupta, O. Jepsen, and O. K. Andersen, Band-structure trend in hole-doped cuprates and correlation with $T_{c\,\max}$, Phys. Rev. Lett. **87**, 047003 (2001).

[55] G. Kresse and J. Furthmuller, Efficient iterative schemes for *ab initio* total-energy calculations using a plane-wave basis set, Phys. Rev. B **54**, 11169 (1996).

[56] G. Kresse and D. Joubert, From ultrasoft pseudopotentials to the projector augmented-wave method, Phys. Rev. B **59**, 1758 (1999).

[57] D. Vanderbilt, Soft self-consistent pseudopotentials in a generalized eigenvalue formalism, Phys. Rev. B **41**, 7892(R) (1990).

[58] J. P. Perdew, K. Burke, and M. Ernzerhof, Generalized gradient approximation made simple, Phys. Rev. Lett. **77**, 3865 (1996).

[59] P. E. Blöchl, Projector augmented-wave method, Phys. Rev. B **50**, 17953 (1994).

[60] W. Ku, T. Berlijn, and C.-C. Lee, Unfolding first-principles band structures, Phys. Rev. Lett. **104**, 216401 (2010).

[61] P. V. C. Medeiros, S. Stafström, and J. Björk, Effects of extrinsic and intrinsic perturbations on the electronic structure of graphene: Retaining an effective primitive cell band structure by band unfolding, Phys. Rev. B **89**, 041407(R) (2014).

[62] A. A. Mostofi, J. R. Yates, G. Pizzi, Y.-S. Lee, I. Souza, D. Vanderbilt, and N. Marzari, An updated version of WANNIER90: A tool for obtaining maximally-localised Wannier functions, Comput. Phys. Commun. **185**, 2309 (2014).

[63] S. Grimme, J. Antony, S. Ehrlich, and S. Krieg, A consistent and accurate *ab initio* parametrization of density functional dispersion correction (DFT-D) for the 94 elements H-Pu, J. Chem. Phys. **132**, 154104 (2010).

[64] V. I. Anisimov, J. Zaanen, and O. K. Anderson, Band theory and Mott insulators: Hubbard U instead of Stoner I, Phys. Rev. B **44**, 943 (1991).

[65] S. L. Dudarev, G. A. Botton, S. Y. Savrasov, C. J. Humphreys, and A. P. Sutton, Electron-energy-loss spectra and the structural stability of nickel oxide: An LSDA+U study, Phys. Rev. B **57**, 1505 (1998).

[66] H. Lu, M. Rossi, A. Nag, M. Osada, D. F. Li, K. Lee, B. Y. Wang, M. G.-Fernandez, S. Agrestini, Z. X. Shen, E. M. Been, B. Moritz, T. P. Devereaux, J. Zaanen, H. Y. Hwang, K.-J. Zhou, and W. S. Lee, Magnetic excitations in infinite-layer nickelates, Science **373**, 213 (2021).

[67] J. Fowlie, M. Hadjimichael, M. M. Martins, D. Li, M. Osada, B. Y. Wang, K. Lee, Y. Lee, Z. Salman, T. Prokscha, J.-M. Triscone, H. Y. Hwang, and A. Suter, Intrinsic magnetism in superconducting infinite-layer nickelates, Nat. Phys. **18**, 1043 (2022).

[68] A. Togo and I. Tanaka, First principles phonon calculations in materials science, Scr. Mater. **108**, 1 (2015).

[69] V. Pardo and W. E. Pickett, Quantum confinement induced molecular correlated insulating state in $La_4Ni_3O_8$, Phys. Rev. Lett. **105**, 266402 (2010).

[70] H. Sakakibara, H. Usui, K. Kuroki, R. Arita, and H. Aoki, Two-orbital model explains the higher transition temperature of the single-layer Hg-cuprate superconductor compared to that of the La-cuprate superconductor, Phys. Rev. Lett. **105**, 057003 (2010).

[71] A. Kreise, B. M. Andersen, A. T. Rømer, I. M. Eremin, and F. Lechermann, Superconducting instabilities in strongly correlated infinite-layer nickelates, Phys. Rev. Lett. **129**, 077002 (2022).

[72] F. Lechermann, Multiorbital processes rule the $Nd_{1-x}Sr_xNiO_2$ normal state, Phys. Rev. X **10**, 041002 (2020).

[73] G. Krieger, L. Martinelli, S. Zeng, L. E. Chow, K. Kummer, R. Arpaia, M. Moretti Sala, N. B. Brookes, A. Ariando, N. Viart, M. Salluzzo, G. Ghiringhelli, and D. Preziosi, Charge and spin order dichotomy in $NdNiO_2$ driven by the capping layer, Phys. Rev. Lett. **129**, 027002 (2022).

[74] H. LaBollita and A. S. Botana, Electronic structure and magnetic properties of higher-order layered nickelates: $La_{n+1}Ni_nO_{2n+2}$ $(n = 4 - 6)$, Phys. Rev. B **104**, 035148 (2021).

[75] J. Karp, A. Hampel, M. Zing, A. S. Botana, H. Park, M. R. Norman, and A. J. Millis, Comparative many-body study of $Pr_4Ni_3O_8$ and $NdNiO_2$, Phys. Rev. B **102**, 245130 (2020).

[76] Z. Wang, C. Zou, C. Lin, X. Luo, H. Yan, C. Yin, Y. Xu, X. Zhou, Y. Wang, and J. Zhu, Correlating the charge-transfer gap to the maximum transition temperature in $Bi_2Sr_2Ca_{n-1}Cu_nO_{2n+4+d}$, Science **381**, 227 (2023).

[77] E. M. Nica, J. Krishna, R. Yu, Q. Si, A. S. Botana, and O. Erten, Theoretical investigation of superconductivity in trilayer square-planar nickelates, Phys. Rev. B **102**, 020504(R) (2020).

[78] Z. Chen, M. Osada, D. Li, E. M. Been, S.-D. Chen, M. Hashimoto, D. Lu, S.-K. Mo, K. Lee, Bai Y. Wang, F. Rodolakis, J. L. McChesney, C. Jia, B. Moritz, T. P. Devereaux, H. Y. Hwang, and Z.-X. Shen, Electronic structure of superconducting nickelates probed by resonant photoemission spectroscopy, Matter **5**, 1806 (2022).

[79] J. Zaanen, G. A. Sawatzky, and J. W. Allen, Band gaps and electronic structure of transition-metal compounds, Phys. Rev. Lett. **55**, 418 (1985).

[80] F. C. Zhang and T. M. Rice, Effective Hamiltonian for the superconducting Cu oxides, Phys. Rev. B **37**, 3759(R) (1988).

[81] P. Worm, L. Si, M. Kitatani, R. Arita, J. M. Tomczak, and K. Held, Correlations tune the electronic structure of pentalayer nickelates into the superconducting regime, Phys. Rev. Mater. **6**, L091801 (2022).